ACS OMEGA

Article

Cite This: ACS Omega 2019, 4, 5304−5309

http://pubs.acs.org/journal/acsodf

Magnéli Phase Titanium Oxide as a Novel Anode Material for Potassium-Ion Batteries

Geon-Woo Lee,[†] Byung Hoon Park,[†] Masoud Nazarian-Samani,[†] Young Hwan Kim,[†] Kwang Chul Roh,[‡] and Kwang-Bum Kim*[,†]

[†]Department of Materials Science and Engineering, Yonsei University, 134 Shinchon-Dong, Seodaemoon-gu, Seoul 120-749, Republic of Korea

[‡]Energy Efficient Materials Team, Energy & Environmental Division, Korea Institute of Ceramic Engineering & Technology, 101, Soho-ro, Jinju 660-031, Republic of Korea

Supporting Information

ABSTRACT: Recently, K-ion batteries (KIBs) have attracted attention for potential applications in next-generation energy storage devices principally on the account of their abundancy and lower cost. Herein, for the first time, we report an anatase TiO_2-derived Magnéli phase Ti_6O_{11} as a novel anode material for KIBs. We incorporate pristine carbon nanotube (CNT) on the TiO_2 host materials due to the low electronic conductivity of the host materials. TiO_2 transformed to Magnéli phase Ti_6O_{11} after the first insertion/deinsertion of K ions. From the second cycle, Magnéli phase Ti_6O_{11}/CNT composite showed reversible charge/discharge profiles with ∼150 mA h g^{-1} at 0.05 A g^{-1}. Ex situ X-ray diffraction and transmission electron microscopy analyses revealed that the charge storage process of Magnéli phase Ti_6O_{11} proceeded via the conversion reaction during potassium ion insertion/deinsertion. The Magnéli phase Ti_6O_{11}/CNT composite electrode showed long-term cycling life over 500 cycles at 200 mA g^{-1}, exhibiting a capacity retention of 76% and a high Coulombic efficiency of 99.9%. These salient results presented here provide a novel understanding of the K-ion storage mechanisms in the extensively investigated oxide-based material for Li-ion batteries and Na-ion batteries, shedding light on the development of promising electrode materials for next-generation batteries.

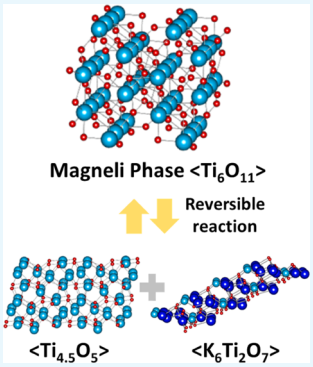

1. INTRODUCTION

Li-ion batteries (LIBs) are primarily used as power sources for electronic devices and vehicles.[1−3] Recently, Na-ion and K-ion batteries (NIBs and KIBs, respectively) have received considerable attention as LIB replacements due to the abundance and low cost of Na and K compared to those of Li resources.[4] As Na and K are in the same group as Li in the periodic table, both NIBs and KIBs share the same "rocking chair" operation principle of LIBs.[5] The redox potential of Na/Na^+ (−2.71 V vs standard hydrogen electrode, noted as SHE) is higher than that of Li/Li^+ (−3.04 V vs SHE); on the other hand, the redox potential of K/K^+ (−2.93 V vs SHE) is closer to that of Li/Li^+. Therefore, KIBs are expected to realize a higher energy density than NIBs due to their wide working potential.[6,7] Since KIBs are still in the initial stage of development, it is necessary to explore and develop novel electrode materials for KIBs.

Recently, carbon-based electrode materials have been investigated for KIBs anode. For example, graphite is known to intercalate with K ion to form a stage I intercalation compound KC_8 with a theoretical capacity of 278 mA h g^{-1}.[8] The studies of carbon anodes have been extended to hard and soft carbons,[9−12] and reduced graphene oxide.[13,14] Inorganic materials such as potassium titanate, Sn, Bi, P, and Sn_4P_3 are also investigated as anode materials for KIBs.[5,15−21]

Anatase TiO_2 has been extensively investigated as an intercalation anode material for LIBs and NIBs, since it has a three-dimensional network crystal structure with empty zigzag channels and intercalation sites for Li and Na ion accommodation and diffusion.[22] However, anatase TiO_2 has not yet been investigated as an anode material for KIBs.

Herein, for the first time, we report TiO_2-derived Magnéli phase Ti_6O_{11} as a novel anode material for KIBs. We incorporate pristine multiwalled carbon nanotubes (CNTs) on TiO_2 host materials due to the low electronic conductivity of the host materials. TiO_2 transformed to Magnéli phase Ti_6O_{11} during the first cycle and Magnéli phase Ti_6O_{11}/CNT composite showed reversible charge/discharge profiles with ∼150 mA h g^{-1} at 0.05 A g^{-1} from the second cycle onward. Ex situ X-ray diffraction (XRD) and transmission electron microscopy (TEM) analyses revealed that the charge storage process of Magnéli phase Ti_6O_{11} proceeded via the conversion reaction during K-ion insertion/deinsertion.

2. RESULTS AND DISCUSSION

Figure S1a shows the X-ray diffraction (XRD) patterns of TiO_2/CNT microspherical composites prepared by spray-

Received: January 6, 2019
Accepted: March 5, 2019
Published: March 14, 2019

DOI: 10.1021/acsomega.9b00045
ACS Omega 2019, 4, 5304−5309

drying method. All the diffraction peaks correspond to the phase-pure anatase TiO_2. The carbon peaks are barely visible, mainly due to the small amount of CNTs in the composites. According to the thermogravimetric analysis (Figure S2), the carbon content in the TiO_2/CNT composites is 9.4 wt %. Figure S1b shows the microspherical morphology of the TiO_2/CNT composites with particle sizes of 2−5 μm. The high-magnification cross-sectional SEM image in Figure S1c shows that CNTs are uniformly distributed throughout the entire composite, resulting in an interconnected nanoporous network in the TiO_2/CNT composites. Figure S1d clearly depicts that the surfaces of pristine CNTs are covered with a ∼10 nm layer of TiO_2 with an intimate contact. In the present study, titanium ethoxide was used as the Ti source to precipitate TiO_2 layer on the pristine CNTs.[23] The inset in Figure S1d illustrates typical high-resolution transmission electron microscopy (HR-TEM) image of the composite with clear lattice fringes of ∼0.35 nm, which corresponds to the (101) interplanar spacing of highly crystalline anatase TiO_2.[22]

Figure 1a shows the initial three charge/discharge profiles of the TiO_2/CNT composite electrode investigated at a current

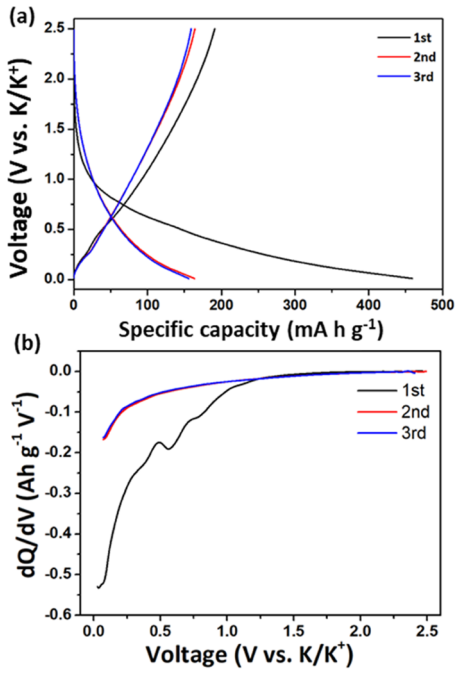

Figure 1. (a) First three charge/discharge curves of TiO_2/CNT composite electrode at 0.05 A g^{-1} and (b) differential capacity versus voltage curves based on the discharge curves of (a).

rate of 0.05 A g^{-1}. The specific capacity of the TiO_2/CNT composite was calculated based on the composite weight. The first discharge and charge capacities were 455 and 191 mA h g^{-1}, respectively, with a Coulombic efficiency of ∼42%. Nevertheless, reversible charge/discharge profiles were observed in the subsequent cycles. To clarify the low Coulombic efficiency of the TiO_2/CNT composite electrode, differential capacity versus voltage curves for the discharge profiles of the TiO_2/CNT composite, bare CNTs, and bare TiO_2 are plotted in Figures 1b, S4b, and S5b, respectively. In the first potassiation process of the TiO_2/CNT composite (Figure 1b), there are three cathodic peaks at 0.9, 0.6, and 0.1 V versus K/K^+. Two peaks at 0.9 and 0.6 V completely disappeared in the subsequent cycles, which could be responsible for the low initial Coulombic efficiency of the TiO_2/CNT composite. The comparison of the differential capacity versus voltage curves of TiO_2/CNT composite with those of CNTs and bare TiO_2 clearly indicates that the two peaks at 0.9 and 0.6 V in Figure 1b correspond to the solid electrolyte interphase (SEI) formation on CNTs (Figure S4b) and the bare TiO_2 (Figure S5b), respectively.

Ex situ XRD analysis was performed to investigate the possible phase transformation of TiO_2 during the initial charge/discharge process. As shown in Figure 2a, Ti_3O_5 (18.8°,

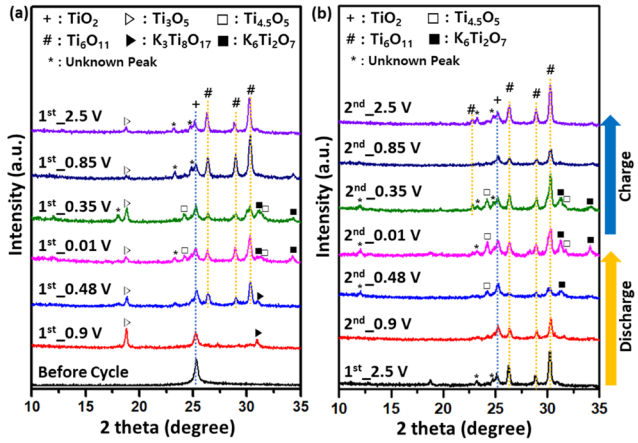

Figure 2. Ex situ XRD patterns of the TiO_2/CNT composite electrode for selected states of charge in the (a) first and (b) second cycle in the potential window of 0.01−2.5 V vs K/K^+ at a current density of 0.05 A g^{-1}.

ICDD No. 01-076-1066) and $K_3Ti_8O_{17}$ (31°, ICDD No. 01-072-1699) newly appeared upon first discharging to 0.9 V. When further discharged to 0.48 V, Magnéli phase Ti_6O_{11} (26.3, 28.9, and 30.3°, ICDD No. 01-085-1058) was observed. At the fully discharged state (0.01 V), additional phases of $K_6Ti_2O_7$ (31.3 and 34.1°; ICDD No. 01-079-1757) and $Ti_{4.5}O_5$ (24.4 and 31.8°; ICDD No. 01-071-6414) were observed. In the subsequent charging to 0.35 V, the XRD patterns showed little difference from those of the fully discharged state. When the electrode was charged to 0.85 V, the $K_6Ti_2O_7$ and $Ti_{4.5}O_5$ diffraction peaks disappeared. At the fully charged state (2.5 V), Magnéli phase Ti_6O_{11} was the major phase with a minor peak of TiO_2, indicating most of the anatase TiO_2 underwent electrochemically driven phase transformation to the Magnéli phase Ti_6O_{11} during the first charge/discharge process. Some unknown peaks were observed (marked as *) during the course of the first cycle.

Figure 2b shows the XRD patterns of Magnéli phase Ti_6O_{11} during the charge/discharge process. When Ti_6O_{11} was discharged to 0.48 V, the formation of $K_6Ti_2O_7$ (31.3°) and $Ti_{4.5}O_5$ (24.4°) was observed. The XRD patterns of the electrode fully discharged to 0.01 V clearly indicate the presence of $K_6Ti_2O_7$ (31.3 and 34.1°) and $Ti_{4.5}O_5$ (24.4 and 31.8°). The remained XRD peaks of Ti_6O_{11} might be due to the unreacted part of Ti_6O_{11}. During the subsequent charging, $K_6Ti_2O_7$ and $Ti_{4.5}O_5$ gradually disappeared and finally Ti_6O_{11} was the major phase in the fully charged state, which indicates the electrochemical and structural reversibility of the Magnéli phase Ti_6O_{11} in the K-ion insertion/deinsertion processes. In the second charge/discharge process cycle, similar unknown peaks were also observed (marked as *).

DOI: 10.1021/acsomega.9b00045
ACS Omega 2019, 4, 5304−5309

Scheme 1. Formation and Potassiation/Depotassiation Mechanism of the Ti_6O_{11}/CNT Composite Electrode

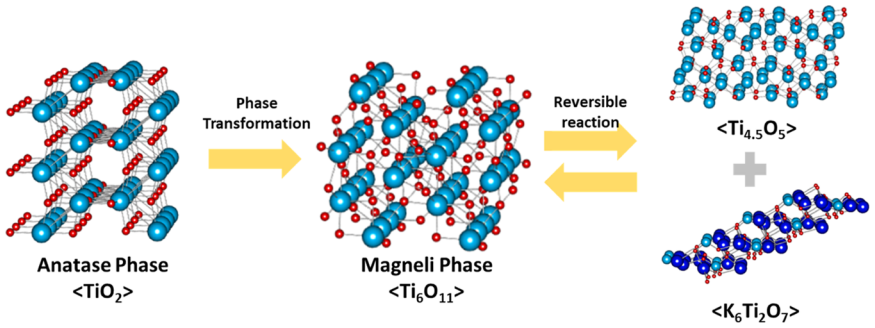

Scheme 1 illustrates two important points regarding the potassiation/depotassiation processes in the Ti_6O_{11}/CNT composite electrode: (i) electrochemically driven phase transformation of TiO_2 to the Ti_6O_{11} Magnéli phase in the first cycle and (ii) reversible potassiation/depotassiation reactions between Magnéli phase Ti_6O_{11} and the discharge products of $K_6Ti_2O_7$ and $Ti_{4.5}O_5$ in the following cycles. This suggests that potassiation/depotassiation reactions of Ti_6O_{11} may proceed through the conversion reaction with K ions, since discharging of Ti_6O_{11} results in the formation of the reduced phase ($Ti_{4.5}O_5$) and the K-ion-rich phase ($K_6Ti_2O_7$) as discharge products. Interestingly, the charge storage mechanism of the anatase TiO_2 anode in LIBs and NIBs is the intercalation/de-intercalation process.[24,25]

When the conversion compounds react with the alkali ions during discharge, a reduced phase and an alkali-ion-rich phase are formed as discharge products. Further, the conversion compounds disintegrate into nm-sized reduced phase particles in the alkali-ion-rich product matrix.[26−28] To examine the discharge products of the Ti_6O_{11}/CNT composite, HR-TEM analyses were carried out for the Magnéli phase Ti_6O_{11} and its fully discharged state. The HR-TEM image of the Ti_6O_{11}/CNT composite shows the crystalline Ti_6O_{11} lattice fringes with a spacing of 0.29, 0.31, and 0.39 nm, which corresponded to the $(\bar{1}01)$, (114), and (101) plane, respectively (Figure S6). A comparison of annular dark field scanning transmission electron microscopy (ADF-STEM) images of the Ti_6O_{11}/CNT composite (Figure 3a) with its fully discharged state (Figure 3b) clearly shows the formation of multiple disintegrated nanodomains with bright contrast in the fully discharged state. The contrast originates from absorption of electrons by the materials and is thus sensitive to heavy-element-rich domains during the ADF-STEM image formation.[28,29] In Figure 3c, energy-dispersive spectroscopy line profiles confirms the high concentration of Ti in the heavy-elements domains. Thus, these disintegrated nanodomains could be reduced-phase nanoparticle product of the conversion reaction. The nano-domain's lattice fringes with a spacing of 0.21 nm in Figure 3d correspond to the $Ti_{4.5}O_5$ (130) plane. Another phase with a lattice spacing of 0.28 nm corresponds to the $K_6Ti_2O_7$ (102) plane. The TEM analysis results in Figure 3 are in good agreement with the XRD results in Figure 2, which supports that the conversion reaction is responsible for the charge storage mechanism of Ti_6O_{11}.

Figure 4a shows the charge/discharge profiles of the Ti_6O_{11}/CNT composite at a current density of 0.05−3 A g^{-1}, and the charge and discharge capacities with increasing current density are summarized in Figure 4b. Specific discharge capacities of the Ti_6O_{11}/CNT composite were 148, 123, 110, 91, 72, 58,

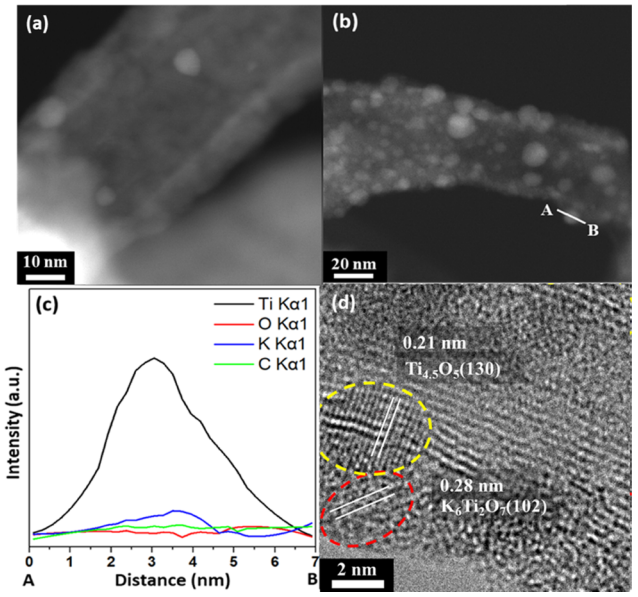

Figure 3. Annular dark field scanning transmission electron microscopy images of Ti_6O_{11}/CNT composite (a) at fully charged state in first cycle and (b) at fully discharged state in second cycle. (c) Energy-dispersive spectroscopy line profile of Ti, O, K, and C along the AB line and (d) HR-TEM image of a fully discharged Ti_6O_{11}/CNT composite.

and 39 mA h g^{-1} at the increasing current densities of 0.05, 0.1, 0.2, 0.5, 1, 2, and 3 A g^{-1}, respectively. Specific discharge capacity of Ti_6O_{11} in the Ti_6O_{11}/CNT composite electrode was calculated using the lever rule of the capacities of Ti_6O_{11}/CNT composite and CNTs

$$C_{composite} = M_{Ti_6O_{11}} \times C_{Ti_6O_{11}} + M_{CNTs} \times C_{CNTs} \quad (1)$$

where $C_{composite}$, $C_{Ti_6O_{11}}$, and C_{CNTs} are the capacities of the composite, Ti_6O_{11}, and CNTs, respectively, and $M_{Ti_6O_{11}}$ and M_{CNT} are the mass ratios of Ti_6O_{11} and CNTs in the composite, respectively. On the basis of the XRD analysis, we assumed that the mass ratio of Ti_6O_{11} in the Ti_6O_{11}/CNT composite is equal to that of TiO_2 in the TiO_2/CNT composite. According to the thermogravimetric analysis (TGA) result in Figure S2, the mass ratio of CNTs in the TiO_2/CNT composite was 9.4 wt %. In our calculation of the specific capacity of Ti_6O_{11}, the mass ratio of Ti_6O_{11} was set at 90.6 wt %. Note that the specific capacities of CNTs were measured to be 134, 108, 83, 60, 41, 31, and 25 mA h g^{-1} at 0.05, 0.1, 0.2, 0.5, 1, 2, and 3 A g^{-1}, respectively (Figure S4d). Finally, specific capacities of Ti_6O_{11} in the composite were

DOI: 10.1021/acsomega.9b00045
ACS Omega 2019, 4, 5304−5309

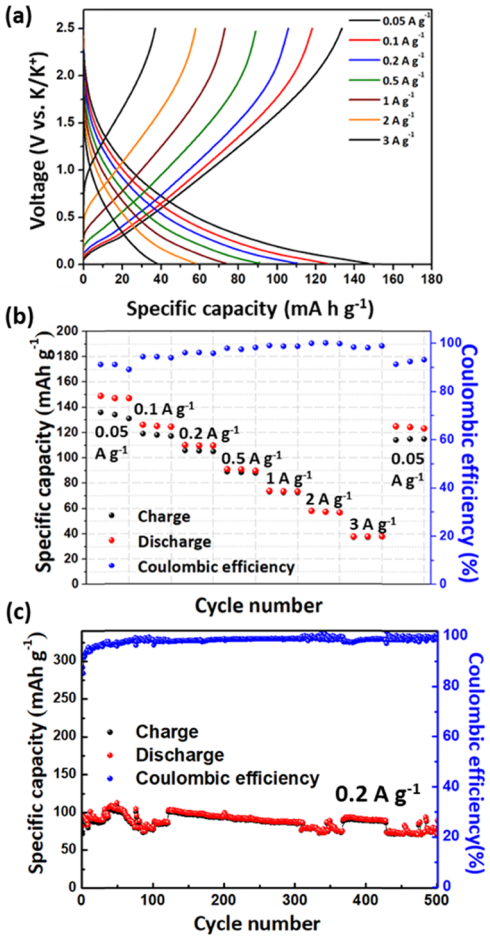

Figure 4. (a) Charge/discharge curves at increasing current density from 0.05 to 3 A g^{-1}, (b) rate capability, and (c) cycling performance at 0.2 A g^{-1} of the Ti_6O_{11}/CNT composite electrode.

calculated to be 135, 113, 102, 85, 68, 55, and 37 mA h g^{-1} at 0.05, 0.1, 0.2, 0.5, 1, 2, and 3 A g^{-1}, respectively.

Interestingly, the electrode composed of bare TiO_2 showed low discharge capacities of 38, 29, 20, and 9−2 mA h g^{-1} at increasing current density of 0.05, 0.1, 0.2, 0.5, and 1 A g^{-1}, respectively, compared to the electrode composed of TiO_2/CNT composite as a starting material. Ex situ XRD analysis was also performed to identify the phases observed during the potassiation/depotassiation of the bare TiO_2 in the initial two cycles (Figure S7). After the first cycle, anatase TiO_2 was found to be the major phase with a minor peak of Magnéli phase Ti_6O_{11}, indicating most of the anatase TiO_2 did not transform to Magnéli Ti_6O_{11} (Figure S7a). From the second cycle on, potassiation of the bare TiO_2 did not induce any changes in the XRD patterns (Figure S7b). Accordingly, no changes in the XRD patterns were observed during the subsequent depotassiation of the bare TiO_2. No information could be obtained about the potassiation/depotassiation of Magnéli Ti_6O_{11} from the XRD patterns in Figure S7 probably due to the very small amount of Magnéli Ti_6O_{11}. In the case of the TiO_2/CNT composite, CNTs provided electron conduction path ways to the anatase TiO_2. Particle size of the anatase TiO_2 in the bare TiO_2 (15−25 nm, Figure S8) is slightly larger than that in the TiO_2/CNT composite (10−15 nm). Thus, the most important difference between the bare TiO_2 and TiO_2/CNT composite is the electron conduction pathways available to the anatase TiO_2 in the composite. It might be responsible for the electrochemically driven phase transformation of the anatase TiO_2 in the composite to the Magnéli phase Ti_6O_{11}.

The Ti_6O_{11}/CNT composite showed stable cyclability over 500 cycles with a capacity retention of 76% and a high Coulombic efficiency of 99.9% at a current density of 0.2 A g^{-1} (Figure 4c). Unstable cycling performance in the early cycles might be due to the instabilities in the conversion reaction and the SEI formation.[10,16,30] At a low current density of 0.05 A g^{-1} (Figure S9a), the Ti_6O_{11}/CNT composite showed a stable cycling behavior after first 20 cycles with a high Coulombic efficiency of 98.6%. Figure S9b shows the XRD patterns of the Ti_6O_{11}/CNT composite electrode at the fully charged state sampled at increasing number of cycles. It is noted that the XRD patterns of Ti_6O_{11} were well maintained, indicating the electrochemical and structural reversibility of the Magnéli phase Ti_6O_{11} in the K-ion insertion/deinsertion processes. It is noted that the intensity of the minor peak of TiO_2 gradually decreased with increasing number of cycles, which suggests that capacity fading might be due to the incomplete transformation of anatase to the Magnéli phase in the initial cycles. Figure S10 shows the plane view SEM image of the morphology of the Ti_6O_{11}/CNT composite electrode in its pristine state (before cycling) and after 500 cycles. There is little change of the morphology of Ti_6O_{11}/CNT composite in pristine state (Figure S10a) and after 500 cycles (Figure S10b). In comparison with oxide-based anode materials for KIBs, the Ti_6O_{11}/CNT composite electrode exhibited improved specific capacity, rate capability, and cyclability (Table S1).

3. CONCLUSIONS

In summary, for the first time, we introduce an anatase TiO_2-derived Magnéli phase Ti_6O_{11}/CNT composite as a novel anode material for KIBs. Our investigation shows that anatase TiO_2 transformed to Magnéli phase Ti_6O_{11} during the insertion/deinsertion of K ions and revealed that Magnéli phase Ti_6O_{11} proceeded K-ion storage process via the conversion reaction. Magnéli phase Ti_6O_{11} showed reversible charge/discharge profiles with ∼150 mA h g^{-1} at 0.05 A g^{-1}. The Magnéli phase Ti_6O_{11}/CNT composite electrode exhibits improved specific capacity, rate capability, and cyclability compared to the state-of-the-art oxide-based anodes. These salient results presented here provide a novel understanding of the K-ion storage mechanisms in the extensively investigated oxide-based material for LIBs and NIBs, shedding light on the development of promising electrode materials for next-generation batteries.

4. METHODOLOGY

4.1. Synthesis of TiO_2/CNT Microspherical Composite.

The TiO_2/CNT microspherical composite were prepared by a one-pot spray-drying process followed by subsequent heat treatment, which is a modification from our previous work.[23] Specifically, the Ti precursor solution was prepared by dispersing titanium ethoxide (2.24 g, Sigma Aldrich) in ethanol (50 mL) with magnetic stirring. The CNTs solutions were prepared by dispersing the as-received MWCNTs (0.1 g, Carbon Nano-material Technology Co., South Korea) in ethanol (50 mL) with sonication for 1 h. The CNT solutions were mixed with the Ti precursor solution under vigorous stirring, followed by the addition of deionized water (50 mL). Hydrolysis and condensation reactions of titanium ethoxide

DOI: 10.1021/acsomega.9b00045
ACS Omega 2019, 4, 5304−5309

started immediately upon the addition of water. Then, the solution was spray-dried at 220 °C using a Buchi Mini spray dryer (Buchi Labortechnik AG, Switzerland). Finally, the spray-dried products were annealed at 450 °C for 3 h under an Ar atmosphere with a heating rate of 5 min^{-1}.

4.2. Characterization. X-ray diffraction (XRD) was performed using a Bruker D8 Advance diffractometer equipped with a Cu Kα radiation radiation from 5 to 80°. For the postmortem analysis of the ex situ XRD samples, the electrodes were detached from the disassembled cells and the electrodes were rinsed in dimethyl carbonate. The electrodes were dried in the Ar glovebox to protect against the moisture in the air. Thermogravimetric analysis (TGA, Mettler Toledo TGA/DSC 1) of TiO_2/CNT microspherical composite was performed in air from 30 to 1000 °C at the heating rate of 10 °C min^{-1}. The morphologies and microstructures of the samples were analyzed by field emission scanning electron microscopy (FE-SEM; JSM-7001F, JEOL Ltd.) and spherical aberration-corrected scanning transmission electron microscopy (Cs-corrected STEM; JEM-ARM 200F, JEOL Ltd.).

4.3. Electrochemical Measurements. The working electrodes were prepared by mixing 80 wt % of TiO_2/CNT microspherical composite as an active material, 10 wt % of carbon black as a conductive agent, and 10 wt % of poly(vinylidene fluoride) (Aldrich) dissolved in *N*-methyl-pyrrolidone (Aldrich) as a binder. Similarly, the bare anatase TiO_2 (P25; ~25 nm) and bare CNTs electrode was also prepared with the same electrode composition. The mixed slurry was coated on a Cu foil and dried at 100 °C for 24 h. The mass loading of electrodes was controlled at 1.2 mg cm^{-2}. The electrochemical properties were measured using coin cells (2032) fabricated with a working electrode and potassium foil as a counter electrode. The electrolyte was a solution of 0.8 M KPF_6 dissolved in a mixture of ethyl carbonate and dimethyl carbonate in a volume ratio of 1:1. The galvanostatic charge–discharge test was performed with a cutoff voltage of 0.01 and 2.5 V using a potentiostat/galvanostat (MPG2, Bio-logic).

■ ASSOCIATED CONTENT

Supporting Information

The Supporting Information is available free of charge on the ACS Publications website at DOI: 10.1021/acsomega.9b00045.

XRD, SEM, TEM, and TGA of TiO_2/CNT composite, TEM image of TiO_2 precursor/CNT composites, electrochemical results for bare CNTs and bare TiO_2, HR-TEM image of fully charged Ti_6O_{11}/CNT composite and bare TiO_2, ex situ XRD patterns of the bare TiO_2 and Ti_6O_{11}/CNT electrode for selected cycles, SEM image of Ti_6O_{11}/CNT composite electrode, summarized table of calculated specific capacity and comparison table of potassium ion storage performance between Ti_6O_{11}/CNT composite electrode and the other reported oxide-based electrode (PDF)

■ AUTHOR INFORMATION

Corresponding Author

*E-mail: kbkim@yonsei.ac.kr.

ORCID

Masoud Nazarian-Samani: 0000-0001-9145-5032

Kwang Chul Roh: 0000-0003-3548-831X

Kwang-Bum Kim: 0000-0003-4624-2104

Notes

The authors declare no competing financial interest.

■ ACKNOWLEDGMENTS

This work was supported by an Energy Efficiency & Resources of the Korea Institute of Energy Technology Evaluation and Planning (KETEP) grant funded by the Korea Government Ministry of Trade, Industry & Energy (MOTIE) (No. 20172420108590) and the Technology Innovation Program or Industrial Strategic Technology Development Program (10062226, development of flexible hybrid capacitor (0.25 mWh/cm^2) composed of graphene-based flexible electrode and gel polymer electrolyte with high electrolyte uptake) funded By the Ministry of Trade, Industry & Energy (MOTIE, Korea).

■ REFERENCES

(1) Park, B. H.; Jeong, J. H.; Lee, G. W.; Kim, Y. H.; Roh, K. C.; Kim, K. B. Highly conductive carbon nanotube micro-spherical network for high-rate silicon anode. *J. Power Sources* **2018**, *394*, 94–101.

(2) Jeong, J. H.; Kim, M. S.; Choi, Y. J.; Lee, G. W.; Park, B. H.; Lee, S. W.; Roh, K. C.; Kim, K. B. Rational design of oxide/carbon composites to achieve superior rate-capability via enhanced lithium-ion transport across carbon to oxide. *J. Mater. Chem. A* **2018**, *6*, 6033–6044.

(3) Wang, M.; Jiang, C.; Zhang, S.; Song, X.; Tang, Y.; Cheng, H. M. Reversible calcium alloying enables a practical room-temperature rechargeable calcium-ion battery with a high discharge voltage. *Nat. Chem.* **2018**, *10*, 667–672.

(4) Xie, K. Y.; Yuan, K.; Li, X.; Lu, W.; Shen, C.; Liang, C. L.; Vajtai, R.; Ajayan, P.; Wei, B. Q. Superior Potassium Ion Storage via Vertical MoS2 "Nano-Rose" with Expanded Interlayers on Graphene. *Small* **2017**, *13*, No. 1701471.

(5) Sultana, I.; Ramireddy, T.; Rahman, M. M.; Chen, Y.; Glushenkov, A. M. Tin-based composite anodes for potassium-ion batteries. *Chem. Commun.* **2016**, *52*, 9279–9282.

(6) Wu, X. Y.; Leonard, D. P.; Ji, X. L. Emerging Non-Aqueous Potassium-Ion Batteries: Challenges and Opportunities. *Chem. Mater.* **2017**, *29*, 5031–5042.

(7) Pramudita, J. C.; Sehrawat, D.; Goonetilleke, D.; Sharma, N. An Initial Review of the Status of Electrode Materials for Potassium-Ion Batteries. *Adv. Energy Mater.* **2017**, *7*, No. 1602911.

(8) Jian, Z.; Luo, W.; Ji, X. L. Carbon Electrodes for K-Ion Batteries. *J. Am. Chem. Soc.* **2015**, *137*, 11566–11569.

(9) Jian, Z. L.; Hwang, S.; Li, Z. F.; Hernandez, A. S.; Wang, X. F.; Xing, Z. Y.; Su, D.; Ji, X. L. Hard-Soft Composite Carbon as a Long-Cycling and High-Rate Anode for Potassium-Ion Batteries. *Adv. Funct. Mater.* **2017**, *27*, No. 1700324.

(10) Chen, C. J.; Wang, Z. G.; Zhang, B.; Miao, L.; Cai, J.; Peng, L. F.; Huang, Y. Y.; Jiang, J. J.; Huang, Y. H.; Zhang, L. N.; Xie, J. Nitrogen-rich hard carbon as a highly durable anode for high-power potassium-ion batteries. *Energy Storage Mater.* **2017**, *8*, 161–168.

(11) Ji, B.; Zhang, F.; Song, X.; Tang, Y. A Novel Potassium-Ion-Based Dual-Ion Battery. *Adv. Mater.* **2017**, *29*, No. 1700519.

(12) Ji, B.; Zhang, F.; Wu, N.; Tang, Y. A Dual-Carbon Battery Based on Potassium-Ion Electrolyte. *Adv. Energy Mater.* **2017**, *7*, No. 1700920.

(13) Share, K.; Cohn, A. P.; Carter, R.; Rogers, B.; Pint, C. L. Role of Nitrogen-Doped Graphene for Improved High-Capacity Potassium Ion Battery Anodes. *ACS Nano* **2016**, *10*, 9738–9744.

(14) Li, J. L.; Qin, W.; Xie, J. P.; Lei, H.; Zhu, Y. Q.; Huang, W. Y.; Xu, X.; Zhao, Z. J.; Mai, W. J. Sulphur-doped reduced graphene oxide sponges as high-performance free-standing anodes for K-ion storage. *Nano Energy* **2018**, *53*, 415–424.

DOI: 10.1021/acsomega.9b00045
ACS Omega 2019, 4, 5304–5309

(15) Kishore, B.; Venkatesh, G.; Munichandraiah, N. K2Ti4O9: A Promising Anode Material for Potassium Ion Batteries. *J. Electrochem. Soc.* **2016**, *163*, A2551−A2554.
(16) Han, J.; Xu, M. W.; Niu, Y. B.; Li, G. N.; Wang, M. Q.; Zhang, Y.; Jia, M.; Li, C. M. Exploration of K2Ti8O17 as an anode material for potassium-ion batteries. *Chem. Commun.* **2016**, *52*, 11274−11276.
(17) Dong, Y.; Wu, Z. S.; Zheng, S. H.; Wang, X. H.; Qin, J. Q.; Wang, S.; Shi, X. Y.; Bao, X. H. Ti3C2 MXene-Derived Sodium/Potassium Titanate Nanoribbons for High-Performance Sodium/Potassium Ion Batteries with Enhanced Capacities. *ACS Nano* **2017**, *11*, 4792−4800.
(18) Huang, J. Q.; Lin, X. Y.; Tan, H.; Zhang, B. Bismuth Microparticles as Advanced Anodes for Potassium-Ion Battery. *Adv. Energy Mater.* **2018**, *8*, No. 1703496.
(19) Sultana, I.; Rahman, M. M.; Ramireddy, T.; Chen, Y.; Glushenkov, A. M. High capacity potassium-ion battery anodes based on black phosphorus. *J. Mater. Chem. A* **2017**, *5*, 23506−23512.
(20) Zhang, W.; Mao, J. F.; Li, S. A.; Chen, Z. X.; Guo, Z. P. Phosphorus-Based Alloy Materials for Advanced Potassium-Ion Battery Anode. *J. Am. Chem. Soc.* **2017**, *139*, 3316−3319.
(21) Li, N.; Zhang, F.; Tang, Y. Hierarchical T-Nb2O5 nanostructure with hybrid mechanisms of intercalation and pseudocapacitance for potassium storage and high-performance potassium dual-ion batteries. *J. Mater. Chem. A* **2018**, *6*, 17889−17895.
(22) Xu, Y.; Lotfabad, E. M.; Wang, H. L.; Farbod, B.; Xu, Z. W.; Kohandehghan, A.; Mitlin, D. Nanocrystalline anatase TiO2: a new anode material for rechargeable sodium ion batteries. *Chem. Commun.* **2013**, *49*, 8973−8975.
(23) Lee, G. W.; Kim, M. S.; Jeong, J. H.; Roh, H. K.; Roh, K. C.; Kim, K. B. Comparative Study of Li4Ti5O12 Composites Prepared withPristine, Oxidized, and Surfactant-Treated Multiwalled Carbon Nanotubes for High-Power Hybrid Supercapacitors. *ChemElectroChem* **2018**, *5*, 2357−2366.
(24) Li, W.; Fukunishi, M.; Morgan, B. J.; Borkiewicz, O. J.; Chapman, K. W.; Pralong, V.; Maignan, A.; Lebedev, O. I.; Ma, J. W.; Groult, H.; Komaba, S.; Damboumet, D. A Reversible Phase Transition for Sodium Insertion in Anatase TiO2. *Chem. Mater.* **2017**, *29*, 1836−1844.
(25) Wu, L. M.; Bresser, D.; Buchholz, D.; Giffin, G. A.; Castro, C. R.; Ochel, A.; Passerini, S. Unfolding the Mechanism of Sodium Insertion in Anatase TiO2 Nanoparticles. *Adv. Energy Mater.* **2015**, *5*, No. 1401142.
(26) Lin, F.; Nordlund, D.; Weng, T. C.; Zhu, Y.; Ban, C. M.; Richards, R. M.; Xin, H. L. Phase evolution for conversion reaction electrodes in lithium-ion batteries. *Nat. Commun.* **2014**, *5*, No. 3358.
(27) Ryu, W. H.; Shin, J.; Jung, J. W.; Kim, I. D. Cobalt(II) monoxide nanoparticles embedded in porous carbon nanofibers as a highly reversible conversion reaction anode for Li-ion batteries. *J. Mater. Chem. A* **2013**, *1*, 3239−3243.
(28) Wang, F.; Robert, R.; Chernova, N. A.; Pereira, N.; Omenya, F.; Badway, F.; Hua, X.; Ruotolo, M.; Zhang, R. G.; Wu, L. J.; Volkov, V.; Su, D.; Key, B.; Whittingharn, M. S.; Grey, C. P.; Amatucci, G. G.; Zhu, Y. M.; Graetz, J. Conversion Reaction Mechanisms in Lithium Ion Batteries: Study of the Binary Metal Fluoride Electrodes. *J. Am. Chem. Soc.* **2011**, *133*, 18828−18836.
(29) Luo, L.; Wu, J. S.; Xu, J. M.; Dravid, V. P. Atomic Resolution Study of Reversible Conversion Reaction in Metal Oxide Electrodes for Lithium-Ion Battery. *ACS Nano* **2014**, *8*, 11560−11566.
(30) Luo, W.; Wan, J.; Ozdemir, B.; Bao, W.; Chen, Y.; Dai, J.; Lin, H.; Xu, Y.; Gu, F.; Barone, V.; Hu, L. Potassium Ion Batteries with Graphitic Materials. *Nano Lett.* **2015**, *15*, 7671−7677.

DOI: 10.1021/acsomega.9b00045
ACS Omega 2019, 4, 5304−5309